Advanced Functional Materials

ADVANCED FUNCTIONAL MATERIALS
www.afm-journal.de

RESEARCH ARTICLE OPEN ACCESS

Thermo-Mechanically Recyclable Smart Textiles from Circularly Knitted Liquid Crystal Elastomer Fibers

Xue Wan[1,2] | Tongxiang Deng[3] | Linda Plaude[4] | Bo Gao[3] | Siyao Chen[3] | Fabien Sorin[2] | Kaspar M. B. Jansen[4] | Kun Zhou[5] | Albert P. H. J. Schenning[1,6]

[1]Stimuli-responsive Functional Materials and Devices, Department of Chemical Engineering and Chemistry, Eindhoven University of Technology, Eindhoven, The Netherlands | [2]Institute of Materials, École Polytechnique Fédérale de Lausanne, Lausanne, Switzerland | [3]National Key Laboratory of Science and Technology on Advanced Composites in Special Environments, Harbin Institute of Technology, Harbin, China | [4]Faculty of Industrial Design Engineering, Delft University of Technology, Delft, The Netherlands | [5]School of Mechanical and Aerospace Engineering, Nanyang Technological University, Singapore, Singapore | [6]Institute for Complex Molecular Systems (ICMS), Eindhoven University of Technology (TU/e), Eindhoven, The Netherlands

Correspondence: Albert P. H. J. Schenning (a.p.h.j.schenning@tue.nl)

Received: 18 November 2025 | **Revised:** 20 January 2026 | **Accepted:** 30 January 2026

Keywords: fiber actuators | liquid crystal elastomers | photoresponsive actuators | smart textiles | thermo-mechanical recycling

ABSTRACT

Liquid crystal elastomer (LCE) fiber actuators are promising candidates for smart textiles owing to their reversible large-stroke actuation and high aspect ratios. However, current LCEs require ultraviolet (UV) curing and are not recyclable. In addition, research is mainly focused on flat knitted thermo-responsive textiles. Here, a scalable recycling route for smart LCE textiles is developed by melt-extruding a thermoplastic LCE containing a near-infrared photothermal dye. The LCE fibers exhibit ~30% reversible actuation strain and display light-driven rolling motions with left- or right-turning trajectories according to their programmed twist handedness. Using commercial knitting machines, multi-material plain- and rib-knit textiles are fabricated that exhibit in-plane contraction and out-of-plane deformations including bending and twisting under thermal and photo stimuli. Circularly knitted tubular structures exhibit reversible contraction in both radial and axial directions, reaching approximately 16% in outer diameter, 19% in inner diameter, and 14% in length, enabling applications in autonomous climbing, controlled liquid release, and micro pumping. Finally, thermo-mechanical recycling yields recycled fibers and both flat and circularly knitted textile structures with nearly unchanged actuation performance and comparable mechanical properties, demonstrating robust recyclability. Our results demonstrate the creation of smart textiles that are simultaneously intelligent in function and sustainable in design.

1 | Introduction

Growing demand for intelligent systems in healthcare and personal comfort has driven a surge of interest in adaptive and functional fabrics [1, 2]. This trend has led to the emergence of smart textiles capable of sensing, actuating, and adapting to environmental stimuli such as heat [3, 4], light [5, 6], electric fields [7, 8], and magnetic fields [9]. The integration of stimuli-responsive materials into textiles marks a transformative advancement, enabling dynamic behaviors that far exceed the capabilities of conventional fabrics. These next-generation textiles hold great promise for various applications, including soft robotics [10, 11], responsive clothing [12, 13], and wearable biomedical devices [14, 15].

Sustainability and circularity are becoming key priorities in the textile industry, with a growing policy emphasis on textile waste prevention and fiber recycling [16]. In 2024, global fiber

production reached ~132 million tonnes, yet only ~7.6% was recycled, and less than 1% came from textile-to-textile recycled fibers [17]. To address this gap, mechanical and chemical recycling routes are being actively explored [18]. Among them, thermo-mechanical recycling, a variant of mechanical recycling, integrates mechanical breakdown of the material, typically by shredding or grinding, with subsequent melting to enable reprocessing while largely preserving the chemical structure [19, 20]. This approach is particularly attractive for textiles made from thermoplastic fibers, owing to its potential to deliver high-quality fibers at low cost. Most textile-recycling studies focus on static fabrics and assess recyclability using metrics such as yield, composition, and polymer quality [21, 22]. It remains challenging to create smart textiles that are simultaneously intelligent in function and sustainable in design.

Among stimuli-responsive materials, liquid crystal elastomers (LCEs) combine the soft elasticity of elastomers with the anisotropic properties of liquid crystals [23, 24]. Their reversible, large-stroke actuation and high aspect ratios make LCE fibers ideal building blocks for smart textile actuators, which have been fabricated via knitting [25–27], weaving [28–30], braiding [31], and embroidery [32]. However, current smart textiles made from LCE fibers rely on UV curing and permanently cross-linked networks, severely limiting reprocessing and recycling. While supramolecular [33] and dynamic covalent chemistries [34, 35] can enable network rearrangement, prior efforts have primarily focused on reconfigurability rather than recyclability with retention of mechanical and actuation performance. Recyclable LCE concepts have been demonstrated mainly in simple, non-textile formats [36–38], while recycling strategies with quantified performance retention for LCE fibers and textile actuators remain unrealized. Additionally, existing LCE textiles are mostly limited to planar knits and two-dimensional (2D) woven architectures with limited post-fabrication programmability. Further exploration is needed to unlock a broader range of functionalities and applications.

Recently, we have reported the preparation of melt-extruded thermoplastic LCE fiber actuators [33, 39]. We now employ this platform to produce stimuli-responsive fibers for smart recyclable textiles. The fibers exhibit a large actuation force of 0.09 N under near-infrared (NIR) illumination. The fibers are compatible with commercial knitting machines, enabling fabrication of diverse multi-material LCE textiles that exhibit reversible actuation modes, including in-plane 2D contraction and out-of-plane three-dimensional (3D) bending and twisting. Using a simple hand-knitting method, circularly knitted 3D tubular structures show reversible, unique contraction in both radial and axial directions for autonomous climbing, liquid release, and micro-pumping applications. The dynamic hydrogen-bonding networks enable the LCE textiles to be reprogrammed into arbitrary configurations. Finally, simple thermo-mechanical recycling achieves recyclability of pristine LCE fibers with nearly unchanged actuation performance and comparable mechanical properties. The recycled fibers can be processed on commercial knitting machines to produce 2D textiles and by hand knitting to create 3D tubular structures, while their actuation performance remains robust after recycling.

2 | Results and Discussion

2.1 | Preparation of the LCE Fibers

To fabricate the LCE fibers, a thermoplastic polythiourethane (PTU) LCE material consisting of 90 wt.% "soft" liquid crystal segments and 10 wt.% "hard" hydrogen-bonding thiourethane segments was synthesized using a previously reported one-pot method (Figure 1a; Figure S1) [40]. This formulation with a high fraction of mesogenic LC segments was selected to enable large actuation strain in the resulting fibers. Subsequently, 1 wt.% photothermal dye, Lumogen IR 765, was added to the PTU polymer, yielding a homogeneous, green-colored mixture referred to as the PTU–IR composite (Figure S2). The low dye content enables efficient photothermal conversion while minimizing impacts on melt processability and the intrinsic thermal transitions of the PTU LCE. The crude PTU–IR composite shows a glass transition temperature (T_g) of −22°C and a melting temperature (T_m) of 170°C (Figure S4). Above 130°C, the degree of hydrogen bonding diminishes significantly, thereby enabling alignment reprogramming of the soft segments (vide infra) [39]. The molten PTU–IR composite exhibits non-Newtonian fluid behavior, as indicated by a decrease in apparent viscosity with increasing shear rate and an apparent yield stress of approximately 600 Pa (Figure S5). Given its T_m and appropriate viscosity range for processing, 190°C was selected as the melt extrusion temperature for the PTU–IR LCE fibers. A total of 60 g of crude polymer was fed into a capillary rheometer, with extrusion and drawing speeds of 0.8 and 53 mm s^{-1}, respectively (Figure 1b; Figure S3). Under the applied drawing force, an LCE fiber with a length of tens of meters was obtained (Figure 1c).

The LCE fiber exhibits a uniform diameter, and the cross-sectional image indicates an average value of 1.3 ± 0.2 mm (Figure 1d). The chemical structure and thermal properties of the LCE fiber and its crude polymer remain nearly identical (Figure S6). In addition, the LCE fiber shows good flexibility and elasticity, as it can be loosely knotted twice along its length without damage (Figure 1e). The scalar order parameter (S) of 0.38, analyzed from the two-dimensional wide-angle X-ray scattering (2D WAXS) measurement, indicates good alignment of "soft" liquid crystal segments along the fiber's axial direction (Figure 1f). Upon heating from 25 to 110°C, the LCE fiber undergoes a length contraction of 31% and a width expansion of 21% when passing the nematic-to-isotropic temperature (T_{NI}) of 84°C due to the loss of mesogen alignment (Figure 1g). The LCE fiber demonstrates good reversible actuation performance over 50 heating–cooling cycles (Figure S7a). The actuation force and stress measured under fixed-strain conditions increase upon heating, reaching 0.20 N and 0.20 MPa, respectively, at approximately 100°C (Figure S7b).

2.2 | Actuation of the LCE Fibers

The strong absorption of the dye in the NIR range (Figure S7c) allows for the photothermal actuation of the LCE fiber. Figure 2a shows that the actuation strain increases with NIR light intensity and reaches a maximum value of ~30%. This trend follows the increase in the measured fiber surface temperature

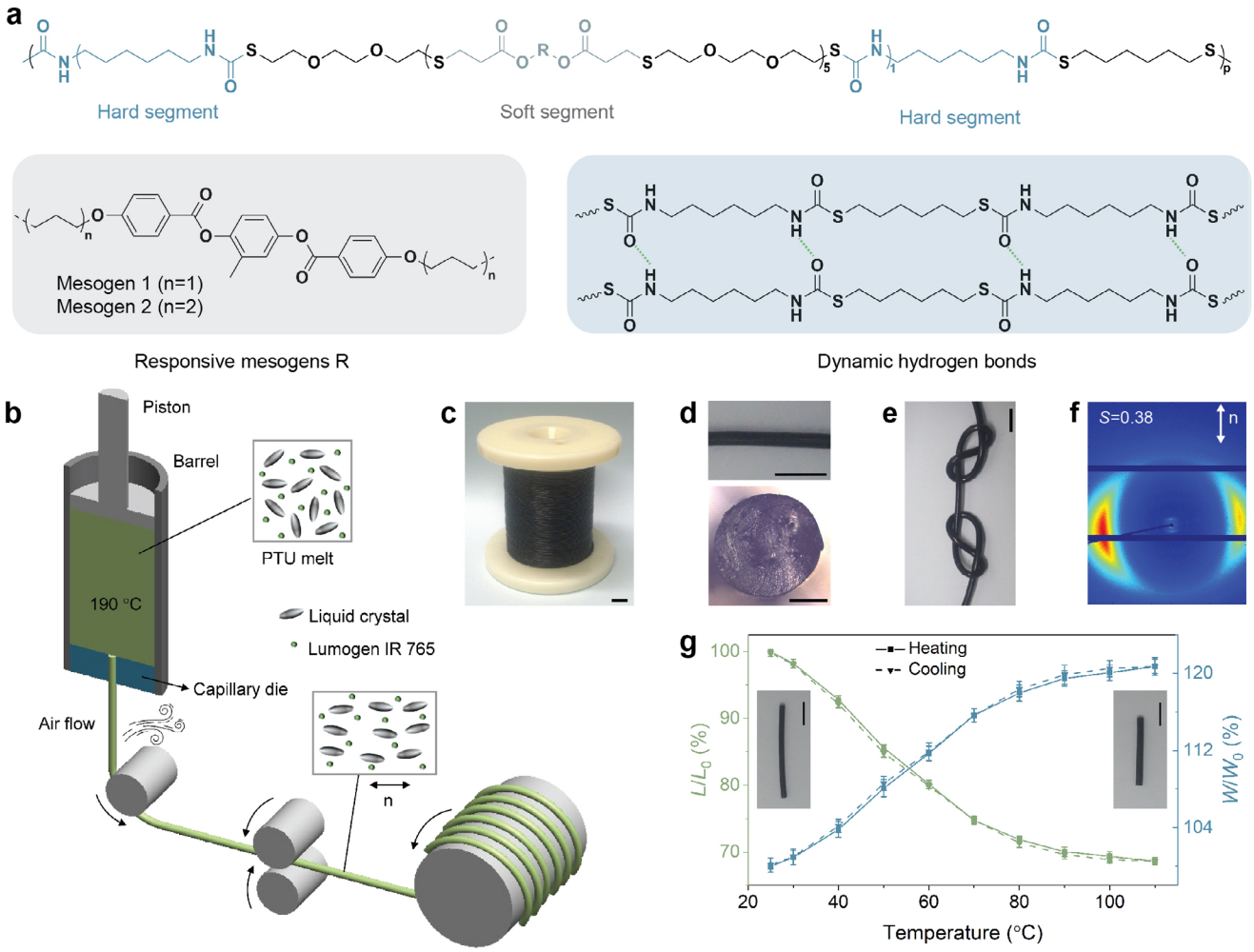

FIGURE 1 | Fabrication of the NIR light–responsive thermoplastic PTU LCE fibers. (a) Chemical structure of the PTU LCE. (b) Schematic of the fiber fabrication process using a capillary rheometer followed by drawing. The liquid crystal mesogens are aligned along the fiber's axial direction. (c) Tens-of-meters-long LCE fibers. Scale bar, 1 cm. (d) Longitudinal and cross-sectional views of the LCE fiber. Scale bars, 5 mm (top) and 500 μm (bottom). (e) Demonstration of the fiber flexibility via knotting. Scale bar, 5 mm. (f) 2D X-ray diffraction pattern of the LCE fiber. The arrow indicates the alignment of mesogens. (g) Length and width changes of the LCE fiber under thermal stimulus. Inset pictures show the fiber at 25 and 110°C, respectively. Scale bars, 5 mm.

under NIR illumination (Figure S8) and is consistent with the fiber's thermally driven actuation at comparable temperatures. The temporal actuation strain rate under the maximum NIR light intensity is shown in Figure S9a. The LCE fiber exhibits stable and reversible light-induced actuation strain of around 27% over 30 cycles (Figure 2b). When the light intensity increases, both the actuation force and stress increase until reaching maximum values of 0.09 N and 0.10 MPa, respectively, at 625 mW cm^{-2} (Figure 2c). Although the actuation stress is moderate, the millimeter-scale fiber can generate a high actuation force, perform significant work, and withstand high loads. We further examine the photoactuation performance of the LCE fibers under different applied stress conditions (Figure 2d). The actuation strain decreases from 28% to 4% with increasing applied stress, while the work capacity increases. Leveraging its soft elasticity and photoresponse, a single LCE fiber was helically wound around a compliant tube and fixed at both ends, functioning as a smart locking device (Figure 2e; Movie S1). When a rod-shaped object was inserted into the tube, illumination with light triggered the contraction of the LCE fiber, reducing the diameter of the compliant tube and securely locking the object. Upon switching off the light, the LCE fiber expanded reversibly, thereby releasing the object.

Next, we turn to reprogramming the LCE fibers to broaden their actuation modes. The dynamic hydrogen-bonding network allows them to be reprogrammed into Z-twist (right-handed) or S-twist (left-handed) configurations by heating and twisting at 130°C for 30 min (Figure 2f). When the twisted LCE fibers were subjected to a load, they exhibited simultaneous compression and untwisting under NIR irradiation (Figure S10), consistent with previous observations in similar twisted thermoset LCE fiber actuators [41]. Next, the fibers were placed on a flat surface in an unconstrained state and irradiated from the right side to evaluate their rolling behaviors. For the straight fiber, the surface closer to the light source experiences a stronger photothermal effect, leading to more pronounced contraction on that side. This induces symmetric bending and generates a net force toward the light source, causing the fiber to roll along a straight path to the right (Movie S2). In contrast, the Z-twist fiber exhibits

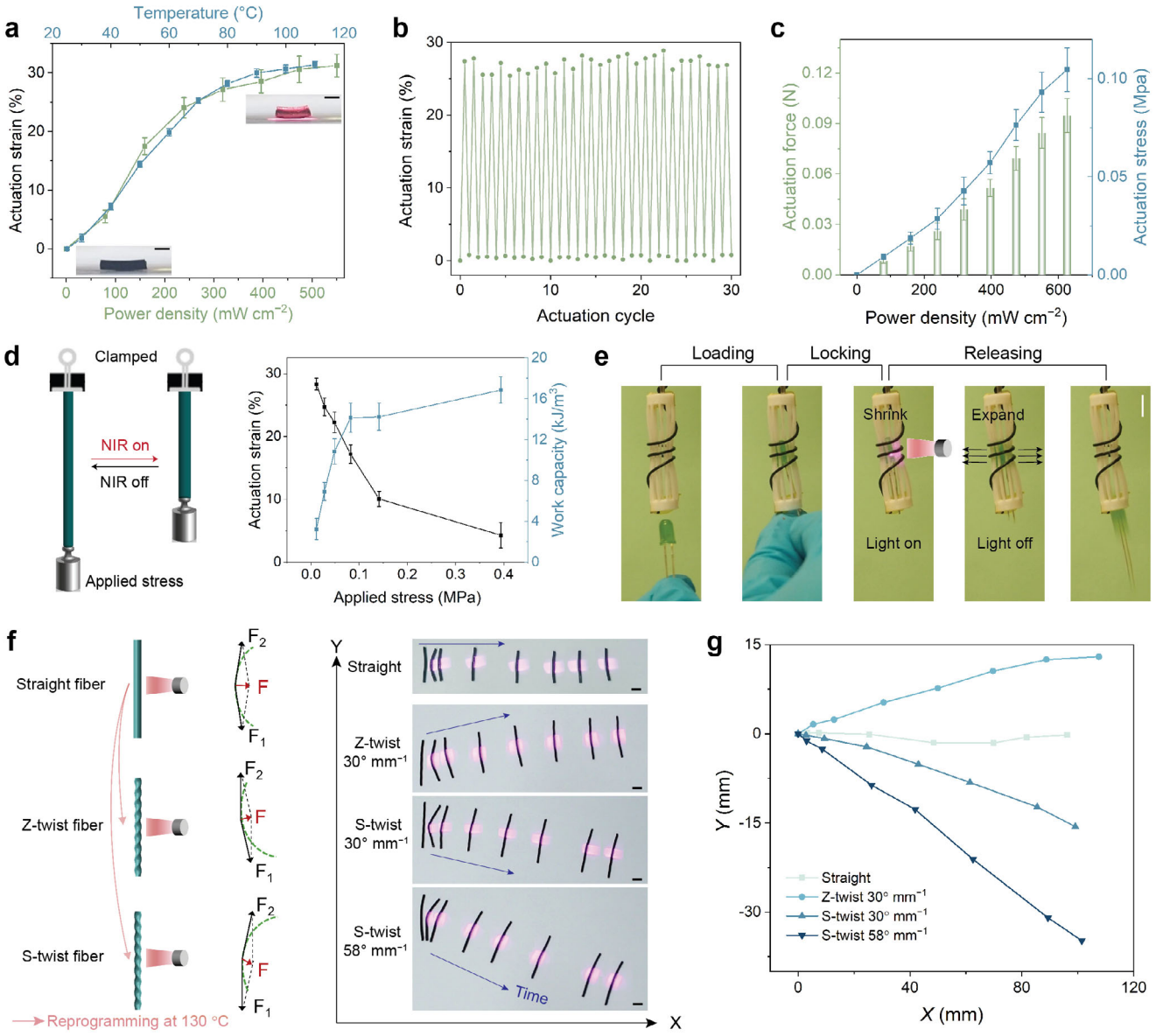

FIGURE 2 | Actuation of the thermoplastic LCE fibers under NIR light. (a) Photothermal actuation strain at different power densities with comparison to thermal actuation. Inset images show the fiber subjected to power densities of 0 and 550 mW cm^{-2}, respectively. Scale bars, 2 mm. (b) Photothermal actuation strain over 30 cycles at a power density of 550 mW cm^{-2}. (c) Output actuation force and stress at different power densities. (d) Schematic diagram and actuation performance under different applied stress levels. (e) Utilization of an LCE fiber wrapped around a compliant tube for locking and releasing a rod-shaped object (LED bulb). Scale bar, 1 cm. (f) Schematic illustration of the force analysis and photographs captured during rolling of the straight, reprogrammed Z-twist, and S-twist fibers. Scale bars, 5 mm. (g) Rolling trajectories of the straight and twisted fibers.

both contraction and untwisting actuation under NIR irradiation, resulting in asymmetric bending and a net force directed upward and to the right, which produces a left-turning motion. Similarly, the S-twist fiber generates a net force directed downward and to the right, resulting in a right-turning motion. These distinct rolling trajectories are attained at rolling speeds in the range of 0.72–1.43 mm s^{-1} (Figure 2g). As the twisting density increases from 30 to 58° mm^{-1}, the S-twist LCE fiber exhibits a larger turning angle. Our results demonstrate light-driven motion of fibers with the direction readily programmed through the fiber's twist handedness. The durability of the as-extruded LCE fibers was evaluated under cyclic thermal and mechanical loading, demonstrating stable and reversible actuation over repeated cycles (Figures S11 and S12).

2.3 | Flat Knitted LCE Textiles

We then investigated the feasibility of knitting the LCE fiber into smart textiles using a commercial domestic flat knitting machine equipped with either single or double knitting beds (Figure 3a; Figure S13a,b). The single bed allows for the fabrication of plain-knit textiles composed of knit loops, while the double bed enables the creation of rib-knit textiles featuring alternating knit and purl loops (Figure 3b). In the plain pattern, interlocking of adjacent loops generally generates a net torque, leading to natural 3D curling deformation of the textile, consistent with typical plain-knit structures [25]. In the rib pattern, the torques generated by alternating knit and purl loops counteract each other, preventing out-of-plane deformation and resulting in a flat,

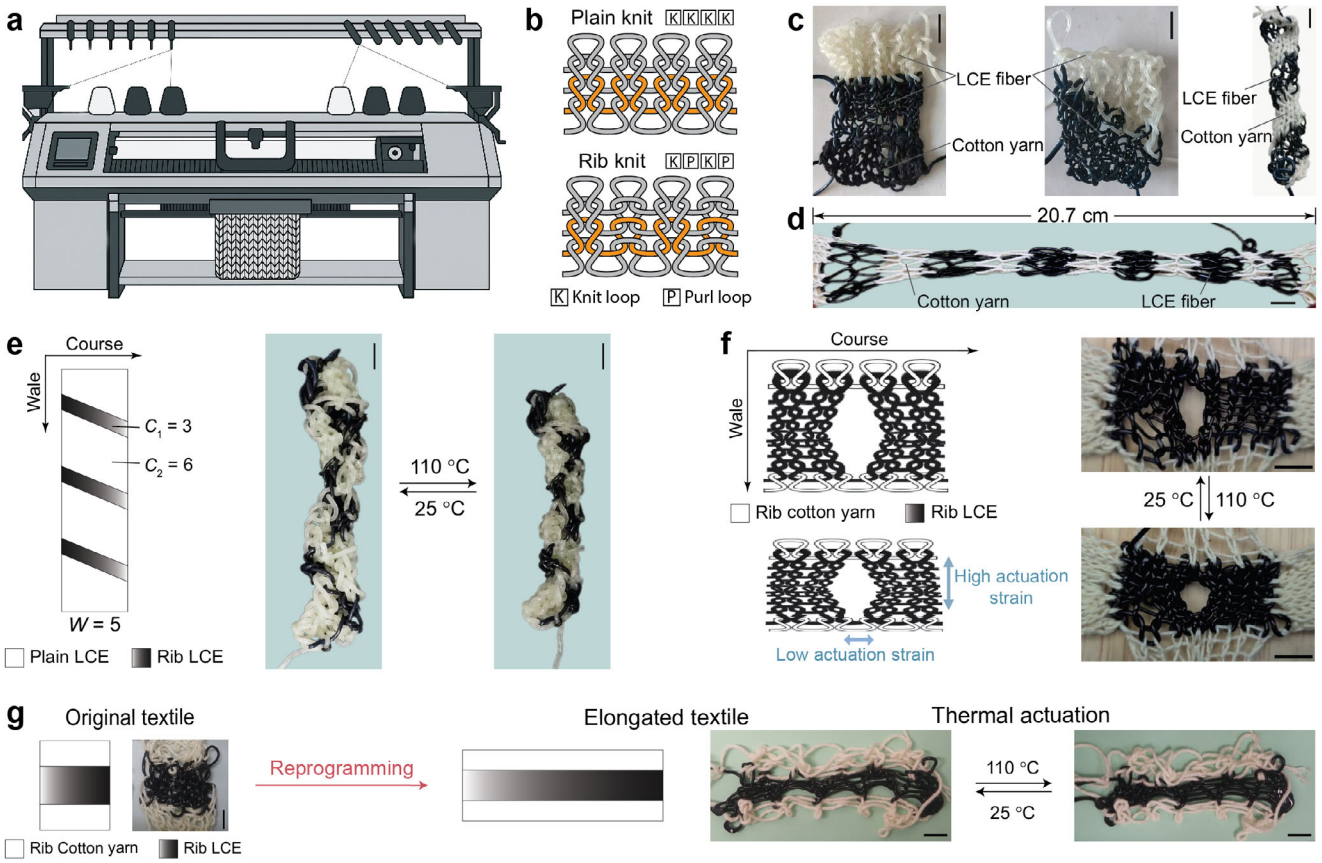

FIGURE 3 | Thermal actuation and reprogrammability of the flat knitted LCE textiles. (a) Schematic of the domestic flat knitting machine. Note that this image was generated using artificial intelligence. (b) Schematic of the plain-knit and rib-knit patterns. (c) Various knitted multi-material LCE textiles composed of LCE fibers (with or without photothermal dye) and commercial cotton yarns. (d) Large-scale plain-knit LCE textile. (e) Slanted multi-material LCE textile combining plain-knit fibers without photothermal dye (white regions) and rib-knit fibers with photothermal dye (black regions), and its corresponding thermal response. *C* and *W* denote the numbers of courses and wales, respectively. (f) Rib-knit LCE textile incorporating a central slit structure and its thermally induced shape change. (g) Reprogrammability of the rib-knit LCE textile into an elongated configuration that exhibits reversible thermal actuation. All scale bars, 10 mm.

contracted textile structure. To further demonstrate the versatility and compatibility of LCE fibers in standard textile fabrication, we explored a multi-material knitting strategy. Various LCE textiles were arranged in both plain and rib patterns using LCE fibers with or without the photothermal dye [33], and with or without commercial cotton yarns (Figure 3c). This approach thus enables diverse fabric styles, color combinations, and pattern designs, highlighting the adaptability of LCE fibers for customizable smart textile architectures.

A plain-knit textile with a length of approximately 21 cm and a width of 1 cm was fabricated (Figure 3d). When heated to 110°C, the LCE fibers contracted, shrinking the knit loops and increasing the accumulated torque, resulting in a more pronounced curling deformation in the black regions (Figure S13c and Movie S3). Overall, the textile demonstrated a diameter shrinkage of 12.2 ± 3.3%. Upon cooling, it fully returned to its original shape. Furthermore, by integrating LCE fibers with and without the photothermal dye, we fabricated a slanted multi-material textile (Figure 3e). In this configuration, white regions represent plain-knit LCE fibers without the photothermal dye, while black regions correspond to rib-knit LCE fibers with the photothermal dye. The textile architecture is defined by the course number (C) and wale number (W), with different course segments (C_1 and C_2) arranged along the wale direction. At room temperature, the textile exhibited an initial spirally twisted shape due to the synergistic effect of curling plain and flat rib patterns. Upon heating to 110°C, the knitted fabric tightened, exhibiting a reversible shrinkage of approximately 18% along the length and 15% along the width (Movie S4). When cooled back to room temperature, the textile fully returned to its original shape, demonstrating excellent reversibility. This multi-material LCE textile enabled selective actuation of the black regions under NIR illumination as only the dye-containing regions were heated and contracted (Figure S14a–b).

Next, we deliberately designed a slit structure in the rib-knit pattern using LCE fibers combined with cotton yarns (Figure 3f). When the two edges of the cotton yarns were slightly stretched and fixed in place, the slit exhibited an elliptical shape. Upon heating to 110°C, the contraction of the LCE fibers caused the black regions to tighten further in-plane (Movie S5). Due to the looser loop density in the wale direction, greater actuation occurred along this axis, resulting in more pronounced contraction. Consequently, the central slit transitioned from an elliptical to a circular shape. Upon cooling to room temperature,

the LCE fibers elongated, and the entire structure returned to its original configuration. Additionally, the dynamic hydrogen-bonding network of thermoplastic LCEs enables reprogramming or reshaping (Figure 3g). The original rib-knit textile provided limited free space for fiber contraction, resulting in constrained actuation. After reprogramming into an elongated configuration, the textile exhibited reversible actuation strains of 13.7% and 6.6% along the length and width directions, respectively, upon heating to 110°C. The elongated textile could be further reprogrammed into a helical configuration (Figures S15 and S16). These findings represent the first demonstration of LCE textiles that can be reprogrammed or reshaped into new geometries based on their existing shapes without disassembling the fibers and re-knitting.

2.4 | Circularly Knitted LCE Tubular Textiles

The long length of the thermoplastic LCE fibers, enabled by our scalable process, allows for hand-knitting in the round on four double-pointed needles to form circular, hollow tubular structures (Figure 4a). Using a plain-knit pattern, the tube diameter was controlled by the stitch count, configured as 4, 6, and 8 stitches per round (sts/round). Figure 4b shows an 8-sts/round LCE tube resting on a cylindrical rod to reveal its tubular geometry. Dynamic mechanical analysis (DMA) in the iso-strain mode reveals the radial compressive actuation force of the knitted tubular structures (Figure 4c). Upon heating, the radial force increases with stitches per round and reaches maximum values of 0.21, 0.31, and 0.40 N for 4-, 6-, and 8-sts/round tubular structures, respectively. Based on their dimensions, the knitted LCE tubes are estimated to produce a compressive pressure of ~1.3–1.8 kPa, comparable to shape memory polymer–based smart stockings and categorized as light by the European Committee for Standardization [42–44].

Next, we investigated the thermal response of the circularly knitted LCE tubular structures by placing them over a thin rod in their natural states (Figure 4d–f). Upon heating, the LCE fiber contracted along its axis and tightened each stitch. As a result, the entire hollow tube exhibited compressive actuation in both the radial and axial directions, unlike previously reported LCE tubes that typically contracted in one direction while expanding in the other [45–48]. Among the tested configurations, the 4-sts/round tube showed the largest actuation strains (Table S2 and Movie S6), delivering an average inner diameter shrinkage of 19.4 ± 1.5%, an outer diameter shrinkage of 16.3 ± 0.9%, and an axial shrinkage of 14.0 ± 0.4% over five cycles. The temporal actuation strain rate of the 4-sts/round tube is shown in Figure S9b. The 6- and 8-sts/round configurations exhibited similar compressive actuation but with smaller strain values. This enhanced actuation of the 4-sts/round tube was attributed to its relatively loose knitting structure and lower inherent structural cohesion, i.e., weaker contractile tendency arising from the knitted configuration compared to the denser 6- and 8-sts/round counterparts.

With the single-fiber model validated (Figure S18), the simulations captured the unique biaxial compressive actuation behavior of the knitted tubes. For the 4-sts/round tube, the simulation predicted an average inner diameter shrinkage of 21.7 ± 4.3%, an outer diameter shrinkage of 14.4 ± 0.6%, and an axial shrinkage of 15.7 ± 0.1%, in good agreement with the experiments (Table S2). However, the simulations of the 6- and 8-sts/round tubes showed larger discrepancies, likely due to geometric variability from hand-knitting, nonuniform loop tension, enhanced inter–fiber contact, friction, and local compression, as well as limitations in capturing the resulting heterogeneous stress and stiffness distributions. These factors become more pronounced at higher stitch counts. Overall, the finite-element simulations captured the experimental actuation behavior, consistent with the mechanism of fiber axial contraction and concomitant transverse expansion that tightens knitted stitches to produce both radial and axial compression. Owing to its large actuation, the 4-sts/round LCE tube was chosen for further studies of possible applications.

2.5 | LCE Tube Demonstrators

The 4-sts/round tube functions as a soft robotic climber that moves via a temperature gradient–driven, sequential anchoring mechanism under cyclic heating between 25 and 110°C (Figure 5a; Movie S7). Initially, the tube remains stationary on the rod due to interfacial friction. Upon heating from the top, a vertical temperature gradient forms and the upper region actuates first. The contraction of LCE fibers shortens the stitches and reduces the local tube diameter, increasing the normal contact pressure and frictional anchoring so that the upper region "grasps" the rod. As the activated region propagates downward, the bottom region subsequently contracts, producing an upward displacement while the upper anchor is maintained. During cooling with airflow applied from top to bottom, the temperature gradient reverses. The upper region expands and releases first, while the lower region remains contracted and serves as the anchor, resulting in a net upward shift after each cycle. Over four cycles, a net displacement of 11.4 mm was recorded (Figure 5b). Slip occurs because recovery during cooling reduces radial compression and weakens anchoring, leading to displacement loss (Figure 5c). To strengthen anchoring, localized photothermal stimulation is introduced. Alternating NIR irradiation at the top and bottom regions increases local contraction and contact pressure, thereby enhancing the anchoring force. As shown in Figure 5d and Movie S7, the combined thermal and photo stimulation minimizes downward slip within each cycle and increases the total upward displacement to 19.9 mm over four cycles (Figure 5c).

The compressive actuation of the LCE tube's diameter also enables its use as a smart liquid dropper. A soft silicone tube was inserted into the inner cavity of a 4-sts/round LCE tube, with one end of the silicone tube vacuum-sealed and the other connected to a glass Pasteur pipette. The silicone tube was initially used like a conventional eye dropper to draw a small amount of blue-colored liquid into the pipette (Figure 5e). Upon heating to 110°C, the LCE tube contracted radially, compressing the soft silicone tube. This mechanical deformation generated internal pressure, which pushed the liquid out of the Pasteur pipette, enabling thermally controlled liquid release (Movie S8). In addition to droplet release, when the distal end of the glass Pasteur pipette was immersed in a Petri dish containing blue-colored liquid, the thermal actuation of the LCE tube enabled repeated uptake and release of the liquid like a smart micro pump, mimicking the operation of a conventional dropper (Figure 5f; Movie S8). As a result, over five heating–cooling cycles, the liquid level in the pipette oscillated

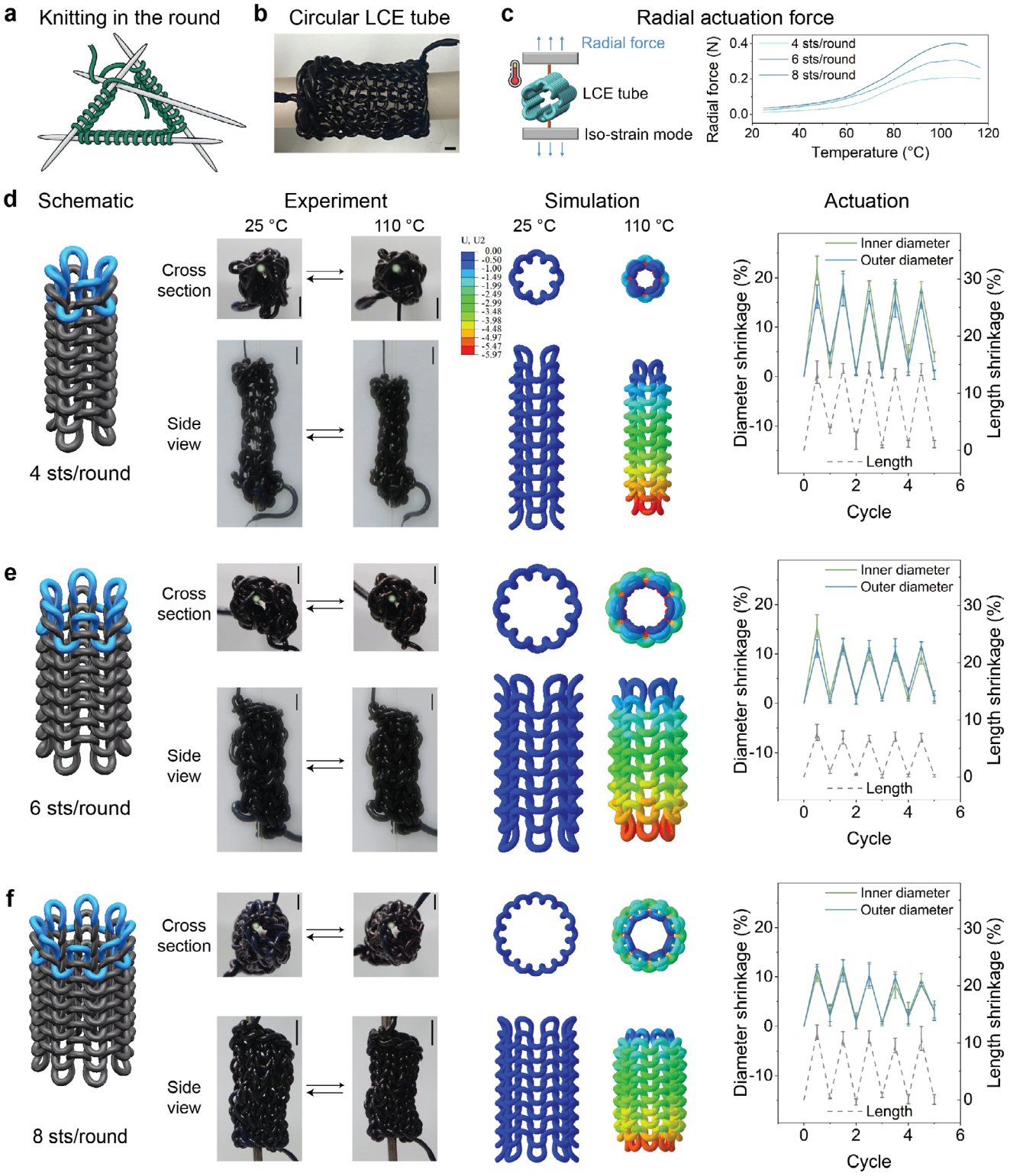

FIGURE 4 | Thermal actuation of the circularly knitted LCE tubular structures. (a) Schematic of the in-the-round knitting process. (b) Photograph of an 8-sts/round LCE tube placed over a cylindrical rod to reveal its hollow structure. (c) Radial compressive actuation force of the tubes upon heating. (d–f) Schematics, experimental images, finite-element simulations, and actuation performance for tubes with 4, 6, and 8 sts/round, respectively. All scale bars, 5 mm.

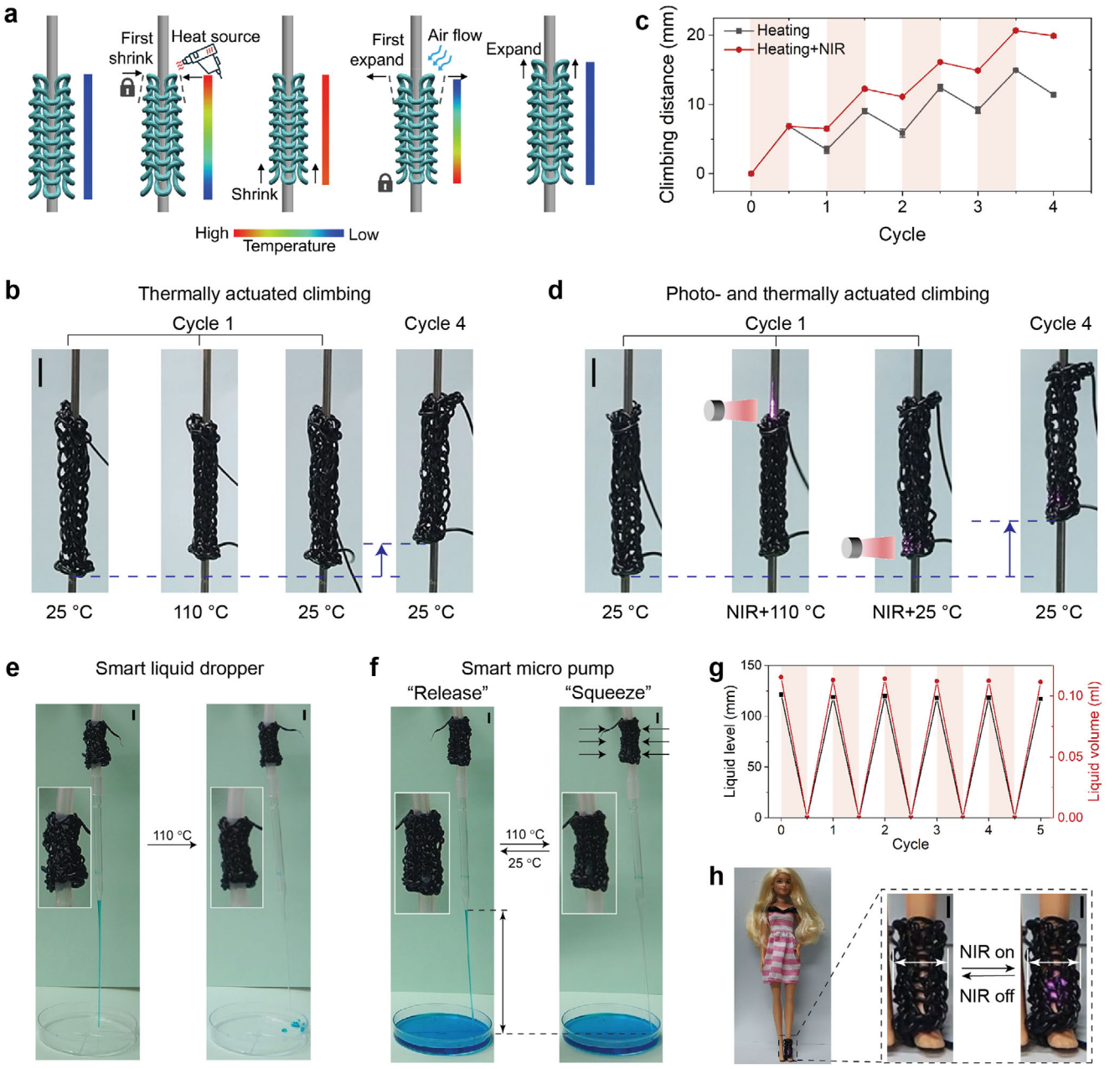

FIGURE 5 | Circularly knitted 4-sts/round LCE tube demonstrators. (a) Schematic illustration of the autonomous climbing mechanism under cyclic heating–cooling stimulation. (b) Thermally actuated climbing behavior, showing the displacement during a complete cycle and the net displacement after four cycles. Scale bar, 10 mm. (c) Comparison of the climbing displacement under thermal and combined thermal–photo stimulation. The red background indicates heating to 110°C or simultaneous heating with NIR irradiation (808 nm). (d) Climbing behavior under simultaneous thermal–photo actuation, showing the displacement during a complete cycle and over four cycles. Scale bar, 10 mm. (e) Thermally induced liquid release enabled by radial compression of the LCE tube. Scale bars, 10 mm. (f) Thermally induced reversible liquid uptake and release by the LCE tube, functioning as a smart micro pump. Scale bars, 10 mm. (g) Evolution of the liquid level and liquid volume during repetitive heating–cooling cycles. The red background indicates heating to 110°C. (h) Localized photoactuation of the LCE tube under NIR irradiation at a power density of 1 W cm^{-2}, demonstrated on the leg of a Barbie doll. Scale bars, 5 mm.

reversibly between 0 and ~120 mm, while the liquid volume varied between 0 and ~0.11 mL (Figure 5g). This reproducible behavior over consecutive actuation cycles demonstrates stable and continuous operation of the knitted LCE tube–based micro pump.

The photothermal dye in the knitted LCE tubes allows for light-responsive behavior both globally and locally. When NIR light with a large irradiation area of around 4.5 × 4.5 cm^2 and a power density of around 1 W cm^{-2} was applied, the LCE tube demonstrated compressive behavior both radially and axially (Figure S17). The LCE tube exhibited compressive actuation of 18.2 ± 0.9% and 13.5 ± 0.5% in the longitudinal and radial directions, respectively, which were comparable to the thermal actuation. In addition to global actuation, NIR illumination enables localized photoactuation. For demonstration, the LCE

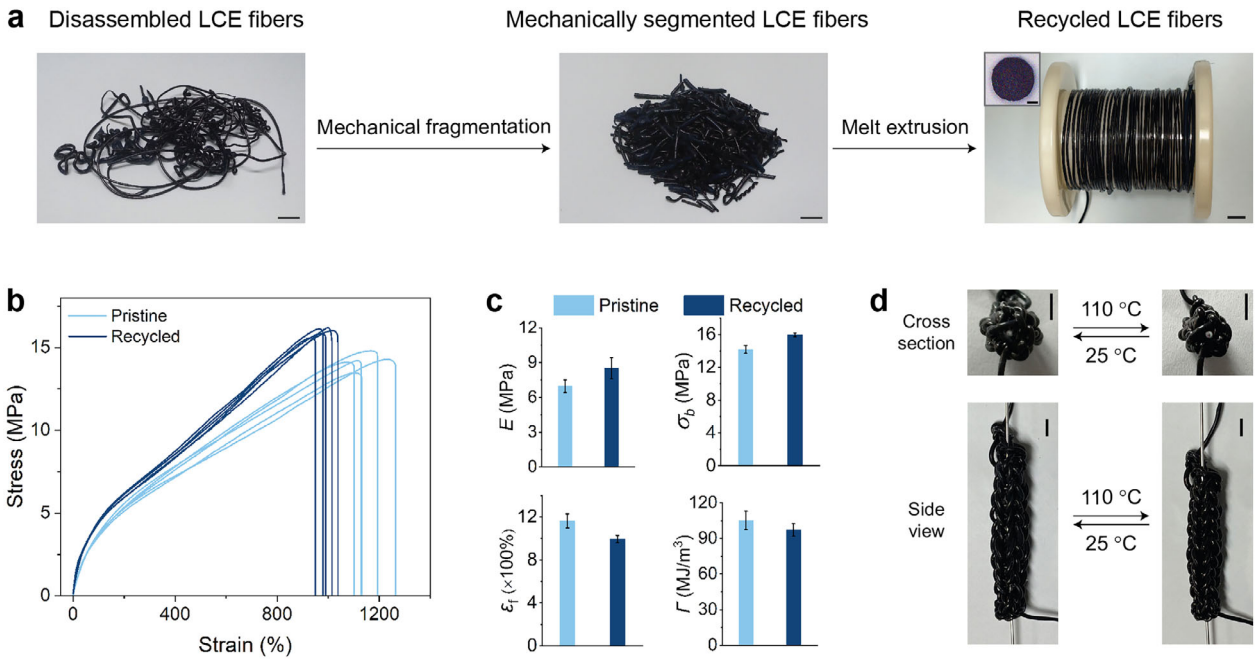

FIGURE 6 | Thermo–mechanical recycling of the LCE textiles and their mechanical and actuation properties. (a) Recycling procedure combining mechanical fragmentation and melt extrusion to obtain the recycled LCE fibers. Scale bars, 10 mm. The inset in the rightmost image shows the cross-sectional view of the recycled fiber. Scale bar, 250 μm. (b) Static tensile stress–strain curves of the pristine and recycled fibers under ambient conditions. (c) Quantitative comparison of the corresponding mechanical properties: E (Young's modulus), σ_b (tensile strength), ε_f (fracture strain), and Γ (toughness). (d) Thermally induced biaxial compressive actuation behavior of a circularly knitted 4-sts/round LCE tubular structure prepared from the recycled fibers. Scale bars, 5 mm.

tube was placed on the leg of a Barbie doll and irradiated locally, where it exhibited pronounced constriction (Figure 5h). This photo-induced compression resembles the functional principle of compression socks, highlighting potential applications in wearable therapeutic devices for circulation management and rehabilitation.

2.6 | Thermal-Mechanical Recycling of the Knitted LCE Textiles

Finally, we investigated the recyclability of the LCE textiles via thermo-mechanical recycling. We disassembled and fragmented the melt-extruded LCE fibers into small segments and subsequently re-fed them into the melt extrusion equipment (Figure 6a). The recycled fibers exhibited a similar appearance to the pristine ones and a slightly smaller diameter of 1.1 ± 0.2 mm (Figure 6a, inset). Figure 6b compares the stress–strain curves of the pristine and recycled fibers under ambient conditions. The recycled fibers exhibit a higher Young's modulus of 8.5 ± 0.9 MPa and tensile strength of 16.0 ± 0.2 MPa, together with a slightly reduced fracture strain of 995.0 ± 33.8% and toughness of 97.1 ± 5.3 MJ m^{-3} (Figure 6c and Table S3). These results indicate that thermo-mechanical recycling increases stiffness and strength at the expense of ductility, while maintaining overall mechanical performance comparable to that of the pristine fibers. The strengthening is likely associated with the slightly reduced fiber diameter and the corresponding higher effective draw ratio during melt extrusion, which can promote processing-induced alignment [49]. Thermogravimetric analysis (TGA) indicates similar thermal stability after recycling (Figure S19).

We then turn to investigate the actuation behavior of the recycled LCE textiles. The recycled fiber maintains ~25% reversible actuation strain over 50 cycles, comparable to pristine fibers, confirming that thermo-mechanical recycling preserves dynamic responsiveness (Figure S20a). The recycled fiber remains compatible with commercial knitting and exhibits reversible textile actuation (Figure S20b and Movie S13). The circularly knitted 4-sts/round LCE tube prepared from the recycled fibers exhibits biaxial compressive actuation, with actuation strains of 14.0 ± 1.4%, 16.1 ± 1.8%, and 15.8 ± 1.0% in the outer diameter, inner diameter, and length directions, respectively, closely matching those obtained from the tubes made of pristine fibers (Figure 6d). These results confirm that the recycled fibers retain their actuation performance after thermo-mechanical recycling, both at the individual fiber level and in textile assemblies (Table S4). Multi-cycle thermo-mechanical recyclability of the LCE material was assessed using hot-pressed films that mimic melt-based thermo-mechanical reprocessing, with actuation strain comparable to the pristine state over repeated cycles (Figure S21). Importantly, this work demonstrates that recyclable LCE fibers can be reprocessed into functional actuating textiles without significant loss of performance, opening a new pathway toward sustainable smart textiles.

3 | Conclusions

In this work, we have developed a scalable, recyclable route for smart textiles by melt-extruding a thermoplastic LCE containing an NIR photothermal dye. The fibers deliver ~30% reversible actuation strain and a large actuation force of 0.09 N

under NIR illumination. Dynamic bonds allow reprogramming, yielding light-driven rolling fibers whose trajectories depend on twist handedness. Using commercial knitting machines, multi-material reprogrammable smart textiles are prepared with designed plain-knit or rib-knit patterns. The textiles demonstrate reversible in-plane 2D contraction and out-of-plane 3D deformations, including bending and twisting in response to temperature or localized light stimuli. Circularly knitted tubular structures exhibit reversible biaxial compressive actuation, with maximum shrinkages of 16.3 ± 0.9% in outer diameter, 19.4 ± 1.5% in inner diameter, and 14.0 ± 0.4% in length. Finite element simulations have been conducted to model the actuation mechanisms, showing good agreement with the experimental results. This unique actuation highlights great potential for autonomous climbing, liquid release, and micro-pumping applications. Finally, the thermo-mechanical recycling strategy achieves reuse of knitted 2D textiles and 3D tubular structures with nearly unchanged performance and comparable mechanical properties, demonstrating robust recyclability. These results demonstrate the creation of smart textiles that are simultaneously intelligent in function and sustainable in design.

4 | Experimental Section

4.1 | Materials

1,4-Bis-[4-(3-acryloyloxypropyloxy)benzoyloxy]-2-methylbenzene (1, ≥97%) and 1,4-bis-[4-(6-acryloyloxyhexyloxy)benzoyloxy]-2-methylbenzene (2, ≥97%) were purchased from Daken Chemical Ltd. 2,2-(Ethylenedioxy)diethanethiol (3, ≥97%), hexamethylene diisocyanate (4, ≥98%), triethylamine (5, ≥99%), and 1,6-hexanedithiol (6, ≥97%) were purchased from Tokyo Chemical Industry. Dimethylphenylphosphine (7, 99%) and *N,N*-dimethylacetamide (DMAc, ≥99%) were obtained from Sigma–Aldrich. The photothermal dye Lumogen 765 was purchased from BASF. Diethyl ether (Et_2O, ≥99.5%) was obtained from Biosolve. All chemicals were used as received without additional purification.

4.2 | Preparation of the Light-Responsive LCE Materials

The synthesis of the PTU LCE followed a reported method (Figure S1) [40]. Diacrylate mesogen 1 (52.81 mmol) and mesogen 2 (52.81 mmol) were dissolved in DMAc (150 mL) in a reaction vessel under argon. After cooling to room temperature, a solution of dithiol 3 (126.74 mmol) and catalyst 7 (0.65 mmol) in DMAc (30 mL) was added sequentially with stirring. After 2 h, a solution of diisocyanate 4 (42.25 mmol) and catalyst 5 (0.99 mmol) in DMAc (14 mL) was introduced, and the mixture was stirred for 15 min. Additional DMAc (193 mL) was added, followed by adding a solution of dithiol 6 (21.12 mmol) in DMAc (13 mL) dropwise, and the reaction mixture was stirred at 60°C overnight. The crude mixture was precipitated with Et_2O (8 L) under continuous stirring, after which the solid was transferred into fresh Et_2O (2 L) and stirred overnight. The final product was obtained by removing the solvent and drying the polymer under vacuum at 50°C overnight. The light-responsive PTU–IR LCE was prepared by first dissolving the PTU polymer in DMAc at 80°C, followed by the addition of 1 wt.% Lumogen 765 with stirring. To ensure uniformity, the mixture was dried and redissolved in DMAc at 80°C. The composite was finally dried under vacuum at 50°C overnight, yielding a dark green solid (Figure S2).

4.3 | Fabrication and Reprogramming of LCE Fibers

Light-responsive LCE fibers were produced on a capillary rheometer equipped with a capillary die (length 10 mm, diameter 2 mm). The PTU–IR composite pellets were fed into a preheating barrel at 180°C, raised to 190°C, held for 2 min, and then extruded. The piston and haul-off speeds were 0.8 mm s^{-1} and 3.2 m min^{-1}, respectively, while a fan was applied for cooling. Further details are provided in Figure S3 and Table S1. Reprogrammed twisted LCE fibers were prepared by fixing one end and rotating the other by a prescribed number of turns, followed by annealing at 130°C for 30 min to lock in the twist. Twist handedness was set by the rotation direction, yielding Z-twist (right-handed) or S-twist (left-handed) fibers. The twist density was controlled by the number of turns and defined as $\tau_0 = \Delta\theta/L_0$, where $\Delta\theta$ represents the rotation angle, and L_0 is the initial fiber length.

4.4 | Fabrication and Reprogramming of Knitted LCE Textiles

Knitted LCE textiles were produced on a domestic knitting machine equipped with either a single bed (Brother KH-868) or a double bed (Brother KH-850) to obtain plain and rib structures (Figure S13). Circularly knitted LCE tubular structures with 4, 6, and 8 sts/round were hand knitted in the round on four double-pointed needles (5 mm diameter). Reprogramming of the knitted rib textile was achieved by stretching the textile at 130°C for 30 min to form an elongated actuator, followed by wrapping it around a rod (8 mm diameter) at 130°C for 30 min to form a helical actuator.

4.5 | Characterization

Differential scanning calorimetry (TA Instruments Q2000) was run from −50 to 200°C at a heating rate of 10°C min^{-1} under nitrogen, and the second heating cycle was analyzed. DMA (TA Instruments Q800) was performed from −50 to 150°C at a heating rate of 5°C min^{-1}, with a 0.01 N preload, a 20 μm amplitude, and a 1 Hz oscillating frequency. TGA (TA Instruments Q50) was conducted from 25 to 800°C at a heating rate of 10°C min^{-1}. ATR-FTIR spectra (Varian 670 IR) were recorded over 4000–650 cm^{-1} at a resolution of 4 cm^{-1}. Rheological tests (AR 2000ex rheometer) were performed using frequency sweeps from 10^{-3} to 10^2 Hz at 190 and 200°C with a strain amplitude of 0.1% and oscillation stress sweeps from 10^0 to 10^4 Pa at 190°C with an angular frequency of 1 rad s^{-1}.

Uniaxial tensile tests of the pristine and recycled fibers (Zwick/Roell) were conducted at a strain rate of 500 mm min^{-1} with a 0.1 N preload. Photoactuation was evaluated under NIR illumination, using 780 nm (80–625 mW cm^{-2}) for fibers and 808 nm (1 W cm^{-2}) for knitted textiles and circular tubes.

Thermally driven actuation stress was monitored by DMA in the iso-strain mode from 20 to 130°C at a heating rate of 5°C min^{-1}, an iso-strain of 1%, and a 0.05 N preload. Light-driven actuation stress was measured under NIR illumination (780 nm, 80–625 mW cm^{-2}).

WAXS was performed on a Ganesha lab instrument equipped with a Pilatus 300 K silicon pixel detector with 487 × 619 pixels of 172 × 172 μm^2 and a Genix-Cu ultralow divergence source. Diffraction patterns were collected with an exposure time of 30 min at a sample-to-detector distance of 89 mm and analyzed to determine the order parameter (S) using the following equation [50]:

$$\mathbf{S} = 1 - 3 \times \frac{\int_0^{\pi/2} I(\theta) \sin\theta \mathbf{cos}^2\theta \mathbf{d}\theta}{\int_0^{\pi/2} I(\theta) \mathbf{sin}\theta \mathbf{d}\theta}$$

where I is the intensity and θ is the angle between a molecular symmetry axis and the director.

4.6 | Recycling of LCE Fibers and Textiles

The pristine and reprogrammed twisted fibers, knitted textiles, and circular tubes were mechanically fragmented into small pieces, vacuum-dried at 50°C overnight, and fed into the capillary rheometer using the same processing parameters to obtain the recycled fibers. The tensile properties and actuation performances of recycled LCE actuators were evaluated.

4.7 | Simulation

Finite element simulations were performed to investigate the deformation behavior of circularly knitted LCE tubes during heating from 25 to 110°C using ABAQUS (Dassault Systèmes, France). The simulation setup mainly consists of geometry import, mesh generation, material property assignment, and the application of interactions and thermal loading. An isotropic elastic model was adopted, with a Young's modulus of 6.98 MPa and a Poisson's ratio of 0.495. The deformation behavior with temperature variation was modeled using orthotropic coefficients of thermal expansion. Taking 25°C as the reference temperature, the coefficients of thermal expansion at 110°C are $-0.00369°C^{-1}$ along the fiber direction and $0.00244°C^{-1}$ perpendicular to the fiber direction. The detailed relationship between strain and temperature is illustrated in Figure 1g. The 3D 10-node quadratic tetrahedral element (C3D10) with a mesh size of 0.5 mm was chosen for the model. To prevent element interpenetration during the deformation, self-contact interactions were imposed on the model.

Acknowledgements

This work was supported by the European Union's Horizon 2020 research and innovation programme under the Marie Skłodowska-Curie grant agreement No 899987, the Institute for Complex Molecular Systems at Eindhoven University of Technology and the Dutch Ministry of Education, Culture and Science (Gravity Program 024.005.020, Interactive Polymer Materials). The authors thank Pengrong Lyu for his help with the WAXS characterization.

Conflicts of Interest

The authors declare no conflicts of interest.

Data Availability Statement

The data that support the findings of this study are available from the corresponding author upon reasonable request.

References

1. K. Dong, X. Peng, and Z. L. Wang, "Fiber/Fabric-Based Piezoelectric and Triboelectric Nanogenerators for Flexible/Stretchable and Wearable Electronics and Artificial Intelligence," *Advanced Materials* 32 (2020): 1902549, https://doi.org/10.1002/adma.201902549.

2. J. Xiong, J. Chen, and P. S. Lee, "Functional Fibers and Fabrics for Soft Robotics, Wearables, and Human–Robot Interface," *Advanced Materials* 33 (2021): 2002640, https://doi.org/10.1002/adma.202002640.

3. X. He, X.-L. Shi, X. Wu, et al., "Three-dimensional Flexible Thermoelectric Fabrics for Smart Wearables," *Nature Communications* 16 (2025): 2523, https://doi.org/10.1038/s41467-025-57889-1.

4. Y. Lin, C. Qu, X. Li, et al., "Sustainable Bi-directional Thermoregulation Fabric for Clothing Microclimate," *Nature Communications* 16 (2025): 6735, https://doi.org/10.1038/s41467-025-62049-6.

5. J. Zhang, T. Chen, M. Zhu, et al., "Scalable, Fast Light-Responsive, and Excellent Color-Retention Fiber-Based Photochromic Wearables for Sustainable Photo-Patterning and Information Security Encryption," *Advanced Functional Materials* 35 (2025): 2415622, https://doi.org/10.1002/adfm.202415622.

6. H. W. Choi, D.-W. Shin, J. Yang, et al., "Smart Textile Lighting/Display System with Multifunctional Fibre Devices for Large Scale Smart Home and IoT Applications," *Nature Communications* 13 (2022): 814, https://doi.org/10.1038/s41467-022-28459-6.

7. L. Zheng, M. Zhu, B. Wu, Z. Li, S. Sun, and P. Wu, "Conductance-stable Liquid Metal Sheath-core Microfibers for Stretchy Smart Fabrics and Self-powered Sensing," *Science Advances* 7 (2021): abg4041, https://doi.org/10.1126/sciadv.abg4041.

8. D.-Y. Lee, S. H. Jeong, A. J. Cohen, et al., "A Wearable Textile-Embedded Dielectric Elastomer Actuator Haptic Display," *Soft Robotics* 9 (2022): 1186–1197, https://doi.org/10.1089/soro.2021.0098.

9. H. Banerjee, A. Leber, S. Laperrousaz, et al., "Soft Multimaterial Magnetic Fibers and Textiles," *Advanced Materials* 35 (2023): 2212202, https://doi.org/10.1002/adma.202212202.

10. D. Shin, K. Kim, S. Y. Yang, J. H. Park, Y. J. Gong, and H. R. Choi, "Woven Fabric Muscle for Soft Wearable Robotic Application Using Two-Dimensional Zigzag Shape Memory Alloy Actuator," *Soft Robotics* 11 (2024): 1008–1019, https://doi.org/10.1089/soro.2023.0171.

11. Z. Zhang, Y. Long, G. Chen, Q. Wu, H. Wang, and H. Jiang, "Soft and Lightweight Fabric Enables Powerful and High-range Pneumatic Actuation," *Science Advances* 9 (2023): adg1203, https://doi.org/10.1126/sciadv.adg1203.

12. Y. Geng, R. Kizhakidathazhath, and J. P. F. Lagerwall, "Robust Cholesteric Liquid Crystal Elastomer Fibres for Mechanochromic Textiles," *Nature Materials* 21 (2022): 1441–1447, https://doi.org/10.1038/s41563-022-01355-6.

13. H. Zhao, X. Qi, Y. Ma, et al., "Wearable Sunlight-Triggered Bimorph Textile Actuators," *Nano Letters* 21 (2021): 8126–8134, https://doi.org/10.1021/acs.nanolett.1c02578.

14. X. Wan, S. Chen, J. Ma, et al., "Multimaterial Shape Memory Polymer Fibers for Advanced Drug Release Applications," *Advanced Fiber Materials* 7 (2025): 1576–1589, https://doi.org/10.1007/s42765-025-00571-4.

15. Y. Wang, C. Sun, and D. Ahmed, "A Smart Acoustic Textile for Health Monitoring," *Nature Electronics* 8 (2025): 485–495, https://doi.org/10.1038/s41928-025-01386-2.

16. European Commission, Communication from the Commission to the European Parliament, the Council, the European Economic and Social Committee and the Committee of the Regions: EU Strategy for Sustainable and Circular Textiles, (2022), https://environment.ec.europa.eu/document/download/74126c90-5cbf-46d0-ab6b-60878644b395_en?filename=COM_2022_141_1_EN_ACT_part1_v8.pdf.

17. Textile Exchange, Materials Market Report 2025, (2025), https://textileexchange.org/knowledge-center/reports/materials-market-report-2025/.

18. J. P. Juanga-Labayen, I. V. Labayen, and Q. Yuan, "A Review on Textile Recycling Practices and Challenges," *Textiles* 2 (2022): 174–188, https://doi.org/10.3390/textiles2010010.

19. F. Mohtaram and P. Fojan, "From Waste to Value: Advances in Recycling Textile-Based PET Fabrics," *Textiles* 5 (2025): 24, https://doi.org/10.3390/textiles5030024.

20. R. B. Baloyi, O. J. Gbadeyan, B. Sithole, and V. Chunilall, "Recent Advances in Recycling Technologies for Waste Textile Fabrics: A Review," *Textile Research Journal* 94 (2023): 508–529, https://doi.org/10.1177/00405175231210239.

21. E. Andini, P. Bhalode, E. Gantert, S. Sadula, and D. G. Vlachos, "Chemical Recycling of Mixed Textile Waste," *Science Advances* 10 (2024): ado6827, https://doi.org/10.1126/sciadv.ado6827.

22. F. A. G. S. Silva, I. Schlapp-Hackl, N. Nygren, et al., "Upcycling of Cellulosic Textile Waste with Bacterial Cellulose via Ioncell® Technology," *International Journal of Biological Macromolecules* 271 (2024): 132194, https://doi.org/10.1016/j.ijbiomac.2024.132194.

23. K. M. Herbert, H. E. Fowler, J. M. McCracken, K. R. Schlafmann, J. A. Koch, and T. J. White, "Synthesis and Alignment of Liquid Crystalline Elastomers," *Nature Reviews Materials* 7 (2021): 23–38, https://doi.org/10.1038/s41578-021-00359-z.

24. C. Ohm, M. Brehmer, and R. Zentel, "Liquid Crystalline Elastomers as Actuators and Sensors," *Advanced Materials* 22 (2010): 3366–3387, https://doi.org/10.1002/adma.200904059.

25. J. Sun, W. Liao, and Z. Yang, "Additive Manufacturing of Liquid Crystal Elastomer Actuators Based on Knitting Technology," *Advanced Materials* 35 (2023): 2302706, https://doi.org/10.1002/adma.202302706.

26. X. Zhang, D. Wu, J. Zhang, et al., "Scalable, Robust and Durable Graphene Oxide@Liquid Crystal Elastomer fiber Actuator with Three-dimensional Complex Photothermal Actuation for Soft Robotics and Smart Textiles," *Chemical Engineering Journal* 519 (2025): 165543, https://doi.org/10.1016/j.cej.2025.165543.

27. Y. Yao, X. Wang, W. Huang, et al., "Low-Temperature Driven Liquid Crystal Elastomer Fibers and Smart Terry Fabrics," *Advanced Functional Materials* (2025): 15319, https://doi.org/10.1002/adfm.202515319.

28. P. E. S. Silva, X. Lin, M. Vaara, M. Mohan, J. Vapaavuori, and E. M. Terentjev, "Active Textile Fabrics from Weaving Liquid Crystalline Elastomer Filaments," *Advanced Materials* 35 (2023): 2210689, https://doi.org/10.1002/adma.202210689.

29. H. Yang, X. Yin, C. Zhang, B. Chen, P. Sun, and Y. Xu, "Weaving Liquid Crystal Elastomer fiber Actuators for Multifunctional Soft Robotics," *Science Advances* 11 (2025): ads3058, https://doi.org/10.1126/sciadv.ads3058.

30. S. Nicita, J. C. Weaver, H. Ishii, and J. Forman, "A Framework for Handweaving Robotic Textiles with Liquid Crystal Elastomer Fibers," *Scientific Reports* 15 (2025): 16883, https://doi.org/10.1038/s41598-025-97835-1.

31. W. Wang, X. Guo, Y. Zhang, et al., "Graded Crosslinked Networks for Tuning Liquid Crystal Elastomer Fibers Performance and Constructing Textile-Based Devices," *Chemical Engineering Journal* 519 (2025): 165248, https://doi.org/10.1016/j.cej.2025.165248.

32. A. P. Martinez, A. Ng, S. H. Nah, and S. Yang, "Active-Textile Yarns and Embroidery Enabled by Wet-Spun Liquid Crystalline Elastomer Filaments," *Advanced Functional Materials* 34 (2024): 2400742, https://doi.org/10.1002/adfm.202400742.

33. S. J. D. Lugger, T. A. P. Engels, R. Cardinaels, T. Bus, D. J. Mulder, and A. P. H. J. Schenning, "Melt-Extruded Thermoplastic Liquid Crystal Elastomer Rotating Fiber Actuators," *Advanced Functional Materials* 33 (2023): 2306853, https://doi.org/10.1002/adfm.202306853.

34. Z. Wang, H. Tian, Q. He, and S. Cai, "Reprogrammable, Reprocessible, and Self-Healable Liquid Crystal Elastomer with Exchangeable Disulfide Bonds," *ACS Applied Materials & Interfaces* 9 (2017): 33119–33128, https://doi.org/10.1021/acsami.7b09246.

35. Y. Yang, Z. Pei, Z. Li, Y. Wei, and Y. Ji, "Making and Remaking Dynamic 3D Structures by Shining Light on Flat Liquid Crystalline Vitrimer Films without a Mold," *Journal of the American Chemical Society* 138 (2016): 2118–2121, https://doi.org/10.1021/jacs.5b12531.

36. C. Li, T. Liu, Y. Li, et al., "Enabling Ultra-High Work Capacity and Scalable Processability of Liquid Crystal Actuators through Densely Entangled Structures," *Advanced Materials* 38 (2026): 13876, https://doi.org/10.1002/adma.202513876.

37. Z. Dong, Y. Wang, J. Chen, et al., "Acylsemicarbazide-Based Supramolecular Liquid Crystal Elastomers: From Molecular Design to Melt-Processing Actuators," *Advanced Functional Materials* (2025): 24643, https://doi.org/10.1002/adfm.202524643.

38. Y. Fan, T. Liu, Y. Li, et al., "One-Step Manufacturing of Supramolecular Liquid-Crystal Elastomers by Stress-Induced Alignment and Hydrogen Bond Exchange," *Angewandte Chemie International Edition* 62 (2023): 202308793, https://doi.org/10.1002/anie.202308793.

39. X. Wan, M. G. Debije, F. Sorin, M. Chen, K. Zhou, and A. P. H. J. Schenning, "Melt-extruded Light-Responsive Amphibious Liquid Crystal Elastomer Fibers with Reprogrammable Actuation Modes," *Chemical Engineering Journal* 505 (2025): 159358, https://doi.org/10.1016/j.cej.2025.159358.

40. S. J. D. Lugger, D. J. Mulder, and A. P. H. J. Schenning, "One-Pot Synthesis of Melt-Processable Supramolecular Soft Actuators," *Angewandte Chemie International Edition* 61 (2022): 202115166, https://doi.org/10.1002/anie.202115166.

41. M. C. Escobar and T. J. White, "Fast and Slow-Twitch Actuation via Twisted Liquid Crystal Elastomer Fibers," *Advanced Materials* 36 (2024): 2401140, https://doi.org/10.1002/adma.202401140.

42. B. Kumar, J. Hu, and N. Pan, "Smart Medical Stocking Using Memory Polymer for Chronic Venous Disorders," *Biomaterials* 75 (2016): 174–181, https://doi.org/10.1016/j.biomaterials.2015.10.032.

43. B. Kumar, J. Hu, N. Pan, and H. Narayana, "A Smart Orthopedic Compression Device Based on a Polymeric Stress Memory Actuator," *Materials & Design* 97 (2016): 222–229, https://doi.org/10.1016/j.matdes.2016.02.092.

44. H. Narayana, J. Hu, B. Kumar, S. Shang, M. Ying, and R. J. Young, "Designing of Advanced Smart Medical Stocking Using Stress-Memory Polymeric filaments for Pressure Control and Massaging," *Materials Science and Engineering: C* 91 (2018): 263–273, https://doi.org/10.1016/j.msec.2018.05.026.

45. Q. He, Z. Wang, Y. Wang, A. Minori, M. T. Tolley, and S. Cai, "Electrically Controlled Liquid Crystal Elastomer–Based Soft Tubular Actuator with Multimodal Actuation," *Science Advances* 5 (2019): aax5746, https://doi.org/10.1126/sciadv.aax5746.

46. N. Najiya, N. Popov, V. S. R. Jampani, and J. P. F. Lagerwall, "Continuous Flow Microfluidic Production of Arbitrarily Long Tubular Liquid Crystal Elastomer Peristaltic Pump Actuators," *Small* 19 (2023): 2204693, https://doi.org/10.1002/smll.202204693.

47. X. Liu, S.-K. Kim, and X. Wang, "Thermomechanical Liquid Crystalline Elastomer Capillaries with Biomimetic Peristaltic Crawling Function," *Journal of Materials Chemistry B* 4 (2016): 7293–7302, https://doi.org/10.1039/C6TB02372J.

48. C. Qi, Y. Guo, Y. Liu, and D. Luo, "Bio-Inspired Untethered Automatic Light Harvesting System Based on Liquid Crystal Elastomers Tubular Actuator," *Advanced Materials Interfaces* 10 (2023): 2202513, https://doi.org/10.1002/admi.202202513.

49. K. Young, F. M. Blighe, J. J. Vilatela, et al., "Strong Dependence of Mechanical Properties on Fiber Diameter for Polymer–Nanotube Composite Fibers: Differentiating Defect from Orientation Effects," *ACS Nano* 4 (2010): 6989–6997, https://doi.org/10.1021/nn102059c.

50. O. Kose, A. Tran, L. Lewis, W. Y. Hamad, and M. J. MacLachlan, "Unwinding a Spiral of Cellulose Nanocrystals for Stimuli-Responsive Stretchable Optics," *Nature Communications* 10 (2019): 510, https://doi.org/10.1038/s41467-019-08351-6.

Supporting Information

Additional supporting information can be found online in the Supporting Information section.

Supporting File: adfm74401-sup-0001-SuppMat.docx.

Supporting File: adfm74401-sup-0002-MovieS1–S9.zip.